NO angular distributions in the photodissociation of $(NO)_2$ at 213 nm: Deviations from axial recoil

A. V. Demyanenko, A. B. Potter, V. Dribinski, and H. Reisler[a)]
Department of Chemistry, University of Southern California, Los Angeles, California 90089-0482

(Received 26 March 2002; accepted 13 May 2002)

Angular distributions of selected rotational states of NO($A\,^2\Sigma^+, \nu=0$) products obtained in the 213 nm photodissociation of $(NO)_2$ have been determined in a molecular beam by using the photofragment ion imaging technique. Specifically, images of NO($A, \nu=0$) products in $N=0$, 11, and 19 have been recorded, for which the maximum energies available to the NO($X\,^2\Pi$) products are 2038, 1774, and 1278 cm^{-1}, respectively. The recoil anisotropy parameter of the photofragments, β_{eff}, decreases significantly at low center-of-mass translational energies from its maximum value of 1.36 ± 0.05, and depends strongly on the rotational angular momentum of the photoproducts. This behavior is described well by a classical model that takes into account the transverse recoil component mandated by angular momentum conservation. For each of the observed NO(A) N states, highly rotating NO(X) levels are produced via planar dissociation, and the angular momenta are established at an interfragment separation of about 2.6 Å. For most of the center-of-mass translational energy range, both corotating and counterrotating fragments are produced, but at the lowest energies, only the latter are allowed. The correlated rotational energy distributions exhibit deviations from the behavior predicted by phase space theory, suggesting that exit-channel dynamics beyond the transition state influences the product state distributions. In this study, a new method for image reconstruction is employed, which gives accurate angular distributions throughout the image plane. © *2002 American Institute of Physics.*
[DOI: 10.1063/1.1490599]

I. INTRODUCTION

Weakly bound molecular complexes are valuable model systems for studying vibrational energy transfer and unimolecular decay.[1,2] The reason is that their bond dissociation energy is generally lower than the energies of the vibrational modes of the strongly bound subunits of the complex, and the large disparity between the intra- and intermolecular vibrational frequencies leads to restricted intramolecular vibrational redistribution (IVR), and to state-specific couplings to the dissociative states. Angular and energy distributions in the fragments are the traditional fingerprints from which mechanisms are inferred, and *correlated* distributions provide even deeper insights into the evolution of the system toward the dissociation asymptote, and the forces and constraints that act in the exit channel.

The dissociation of the nitric oxide dimer, $(NO)_2$, which is formed by the pairing of two $^2\Pi$ radicals, is particularly intriguing, because it belongs to the special family of weakly bound complexes that are *covalently bound*.[3–10] The possible arrangements of the two unpaired electrons, which are located in π^* orbitals in the monomers, in the nearly degenerate molecular orbitals of the dimer, give rise to several close-lying electronic states.[3] Extensive spectroscopic studies have provided detailed information about the ground state structure, bonding, and dissociation dynamics. The ground $1\,^1A_1$ state is bound by $D_0=710\pm15$ cm^{-1},[7] reflecting its covalent character. The equilibrium geometry of the gas phase dimer, determined by microwave spectroscopy, is a *cis*-planar trapezoidal structure of C_{2v} symmetry.[4,5] The N–N bond distance is 2.236 Å, the ONN angle is 99.6°, and the NO bond length is 1.161 Å (about 0.01 Å longer than in the monomer).

In contrast to the extensive work carried out in the time and frequency domains on the IR vibrational predissociation of the dimer,[6–10] little is known about the photodissociation dynamics of the dimer from its electronic excited states. The intense UV absorption spectrum, first reported by Bernstein and Herzberg,[11] is broad and nearly featureless, spanning the range 190–240 nm with a maximum at 205 nm.[12,13] The transition apparently involves the orbital excitation $b_2 \leftarrow a_1$ in C_{2v} symmetry, with the transition dipole moment parallel to the N–N bond.

The UV photodissociation of $(NO)_2$ was first studied by Kajimoto *et al.*[14–18] Experiments at 193 nm revealed two open product channels:

$$(NO)_2 \rightarrow NO(A\,^2\Sigma^+) + NO(X\,^2\Pi), \quad \Delta H = 44\,910\ cm^{-1}, \tag{I}$$

$$(NO)_2 \rightarrow NO(B\,^2\Pi) + NO(X\,^2\Pi), \quad \Delta H = 46\,190\ cm^{-1}. \tag{II}$$

The NO(A) rotational state distributions appeared statistical, and were fit by a constrained version of phase space theory (PST).[18] Other studies showed weak alignment and vector correlations in the NO(A) product, and the authors proposed

a)Electronic mail: reisler@usc.edu

that the dissociation occurred mostly in the plane of the dimer.[15–17] The dynamics were interpreted in terms of a fast, direct dissociation, as indicated by the structureless absorption spectrum, and the large value of the recoil anisotropy parameter, $\beta = 1.0-1.4$.

Studies of $(NO)_2$ photolysis via channel I at 210 nm by femtosecond time-resolved photoelectron spectroscopy showed that $(NO)_2$ dissociation is not direct but stepwise,[19] due possibly to excited state nonadiabatic couplings. It was proposed that the initially prepared state decays nonadiabatically with a lifetime of ≈0.3 ps to a "dark" state or manifold of levels that in turn decays to the products on the longer time scale of ≈0.7 ps. *Ab initio* calculations reveal that in the UV region, both charge-transfer and Rydberg states can be accessed optically, but the exact energies of the states, and the interactions among them, are presently unknown.[3] Thus, the photodissociation processes leading to channels I and II are currently poorly understood, and are the subject of ongoing investigations.[20]

In this paper, we describe our first results on the photodissociation of the NO dimer via reaction I using the velocity map imaging technique. Specifically, we report correlated energy and angular distributions in the $NO(A, \nu = 0)$ fragment following 213 nm dissociation; i.e., at $E_{av1} = 2038\ cm^{-1}$. This energy is sufficient to produce either $NO(X, \nu = 0) + NO(A, \nu = 0)$ or $NO(X, \nu = 1) + NO(A, \nu = 0)$, but not $NO(X, \nu = 0) + NO(A, \nu = 1)$. Images are obtained by monitoring selected rotational levels of $NO(A, \nu = 0)$, from which the correlated energy and angular distributions in $NO(X, \nu = 0,1)$ are determined. The speed-dependent recoil anisotropy parameter, $\beta_{eff}(V)$, is derived from the angular distributions by using,[21]

$$P(\theta, V) \propto \left(\frac{1}{4\pi}\right)[1 + \beta_{eff}(V) P_2(\cos\theta)]. \quad (1)$$

Our work demonstrates strong deviations from fragment axial recoil at low center-of-mass (c.m.) translational energies. The deviations are described with an extended model based on the one used previously to model speed-dependent angular distributions in unimolecular decomposition of triatomic species.[22] This model, which assumes planar dissociation, relates the transverse recoil to angular momentum constraints for fragment pairs with high rotational angular momentum.

II. EXPERIMENTAL METHODS

The experiment involves the generation of $(NO)_2$ in a molecular beam of NO seeded in He, resonance enhanced multiphoton ionization (REMPI) for product $NO(A\ ^2\Sigma^+)$ detection, and photofragment velocity map imaging for recording the velocity and angular distributions of state-selected products. $(NO)_2$ dimers are excited in a single photon transition to above the threshold of reaction I, leading to fast dissociation.

The velocity map imaging arrangement has been described in detail elsewhere.[23] In brief, it consists of an ion-acceleration stage, a 60-cm-long drift tube, and a charge coupled device (CCD) camera that monitors a phosphor screen coupled to a microchannel plate (MCP) ion detector. The ion optics of the ion-acceleration stage is based on a scheme proposed by Parker and Eppink for velocity map imaging,[24] and consists of a repeller, an open extractor electrode (50 mm hole), and an open ground electrode (25 mm hole). At an optimal voltage ratio for the repeller and extractor plates, all ions with the same initial velocity are focused onto the same spot on the MCP detector.

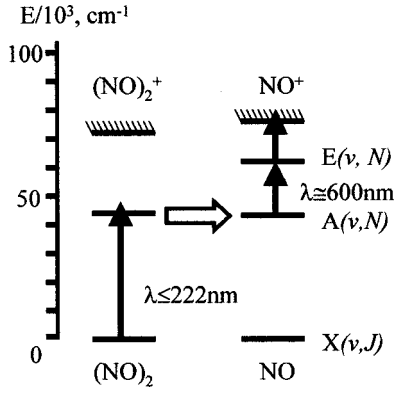

FIG. 1. Energy diagram for the UV dissociation of $(NO)_2$ with subsequent detection of NO(A) fragments by 1+1 REMPI via the $E\ ^2\Sigma^+ \leftarrow A\ ^2\Sigma^+$ transition.

Nitric oxide dimer is formed in a free jet expansion of NO:He gas mixture. A doubly skimmed pulsed molecular beam containing typically 7% of NO seeded in 2.0 atm of He propagates through a hole in the repeller plate. Further downstream, $(NO)_2$ is photolyzed with pulsed, linearly polarized, and mildly focused (f.l.=60 cm lens) UV laser radiation (0.1–0.3 mJ) that intersects the molecular beam at a right angle. Photolysis at 213 nm is achieved by using the frequency-doubled output of an excimer-laser pumped dye laser system (Coumarin 440).

$NO(A\ ^2\Sigma^+)$ photofragments are probed state selectively with the focused output of a Nd:YAG laser pumped dye laser system (Rhodamin 640, 0.2–0.5 mJ; f.l.=50 cm lens) by 1+1 REMPI via the $E\ ^2\Sigma^+ \leftarrow A\ ^2\Sigma^+$ transition at ~600 nm.[16,25,26] The R branch of the transition is used to probe different rotational states of the NO(A) photofragment. Both the $A\ ^2\Sigma^+$ and $E\ ^2\Sigma^+$ states are spectroscopically well characterized, and the low vibrational levels of the A and E states are not predissociative.[25–28] At the employed probe laser intensity, the monitored transitions are saturated,[28] but the results do not change when the laser intensity is lowered by about a factor of 10. The photolysis and probe lasers are both linearly polarized, and introduced coaxially at a right angle to the molecular beam. The polarization of the photolysis light is directed perpendicular to the molecular beam, in a plane parallel to the detector plane. To minimize complications due to vector correlations, the polarizations of the two lasers are fixed parallel to each other. We expect that contamination of the anisotropy parameter by rotational alignment is negligible.[16] The time delay between the pump and probe lasers is kept at 0 ± 5 ns. Typical signals include the summation of $(1-2) \times 10^4$ laser firings. The angular distribution of the fragments reflects predominantly the anisotropy in the photolysis step. Figure 1 shows the probing scheme in relation to the dissociation mechanism.

The correspondence between the measured signal and $(NO)_2$ photolysis is checked in two ways. First, the production of the dimer in the molecular beam is confirmed by detecting $(NO)_2^+$ signals using nonresonant two-photon ionization at 281 nm, and monitoring mass 60.[29] Second, we verify that the dimer is the main source of the NO(A) signal by measuring the dependence of its intensity on NO concentration in the gas mixture (from 2% to 20%). The measured dependence is close to quadratic. By measuring the REMPI spectrum of the NO $A\,^2\Sigma^+ \leftarrow X\,^2\Pi$ transition in mixtures of 7%–20% NO, we estimate that the rotational temperature in the beam is $T_{\rm rot}=3-5$ K.

The main source of background ion signal is non-state-selective ionization of NO(A) fragments by the pump laser 213 nm radiation. Fortunately, it gives only a small contribution to the total signal, and the 600 nm REMPI probe signal is dominant by more than an order of magnitude. To eliminate the contribution from ionization by the pump laser, a subtraction routine is employed, which takes into account the background signal obtained with the pump laser only. Good spatial and temporal overlap of the two laser beams minimizes effects due to ionization by the pump.

III. EXPERIMENTAL RESULTS AND ANALYSIS

Following 213 nm photolysis, images were obtained for rotational levels of NO($A\,^2\Sigma^+, \nu=0$) $N=0,11,19$.[30] The electric field vector **E** of the photolysis laser was maintained parallel to the vertical direction of the image plane, and the product recoil velocities were aligned predominantly in the polar direction of the image. The images were symmetrized and, after background subtraction (see Sec. II), the two-dimensional (2D) projections were converted to three-dimensional (3D) velocity distributions by using the basis set expansion (BASEX) method for image reconstruction.[31]

The BASEX method for reconstructing 3D images with cylindrical symmetry from their 2D projections was developed to enable us to obtain accurate velocity and angular distributions from regions of the image near the center, where reconstruction noise is large in the commonly used inverse Abel transform method (i.e., fast Fourier transform followed by a discrete Hankel transform).[32] The method is based on expanding the projection in a basis set of functions that are analytical projections of known well-behaved functions. The original 3D image can then be reconstructed as a linear combination of these well-behaved functions, which have a Gaussian-type shape, with the same expansion coefficients as the projection. In the process of finding the expansion coefficients, regularization is used to achieve a more reliable reconstruction of noisy projections. The method is efficient and computationally cheap, and is particularly well suited for transforming projections obtained in photoion and photoelectron imaging experiments. The fragment's speed distribution is obtained by analytical integration of the reconstructed image, expressed as a linear combination of basis functions, at each distance from the center over all angles. The angular distributions are directly obtained from the expression of the image in polar coordinates.

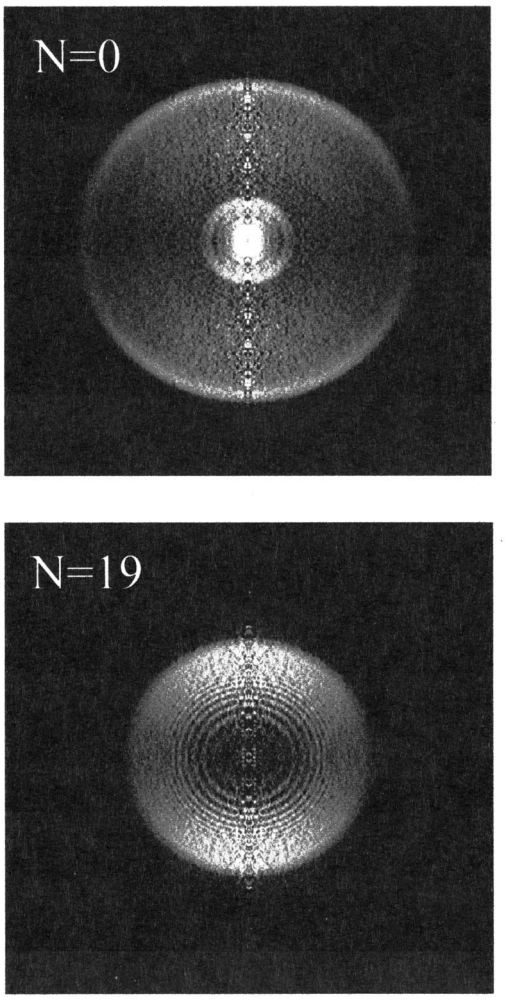

FIG. 2. 2D cuts of the reconstructed images of NO($A\,^2\Sigma^+, \nu=0, N=0$), and NO($A\,^2\Sigma^+, \nu=0, N=19$) obtained from $(NO)_2$ photodissociation at 213 nm. The electric field vector of the photolysis laser is parallel to the vertical direction of the image plane.

Figure 2 shows typical 2D cuts of the reconstructed images of NO($A\,^2\Sigma^+, \nu=0$) fragments probed in the $N=0$ and 19 states. The total excess energy with respect to the channel I threshold is $E_{\rm avl}=2038\ {\rm cm}^{-1}$, and the maximum energies available to the NO(X) products are $E_{\rm max}=2038$ and 1278 $\rm cm^{-1}$ for NO(A) $N=0$ and 19, respectively.

The speed distribution of each NO(A,N) is converted to a translational energy distribution $P(E_t)$ from which the correlated NO(X,Ω,ν,J) internal energy (spin–orbit, vibrational, and rotational, respectively) distribution $P(E_{\rm int})$ can be derived, albeit with loss of state resolution, since several NO($X\,^2\Pi_{1/2,3/2}, \nu, J$) states can contribute to each E_t. While NO(A) fragments are produced only in $\nu=0$, NO(X) fragments correlated with NO($A\,^2\Sigma^+, N=0$) are produced in both $\nu=0$ and 1. The two bright inner rings in Fig. 2 ($N=0$) correspond to NO($X, \nu=1, J$): the intense center ring marks the onset of NO($X\,^2\Pi_{3/2}, \nu=1, J$), and the larger inner ring is associated with NO($X\,^2\Pi_{1/2}, \nu=1, J$). The faint outermost ring corresponds to NO($X\,^2\Pi_{1/2,3/2}, \nu=0, J$). Similar images are obtained for the other two NO(A) states $N=11$

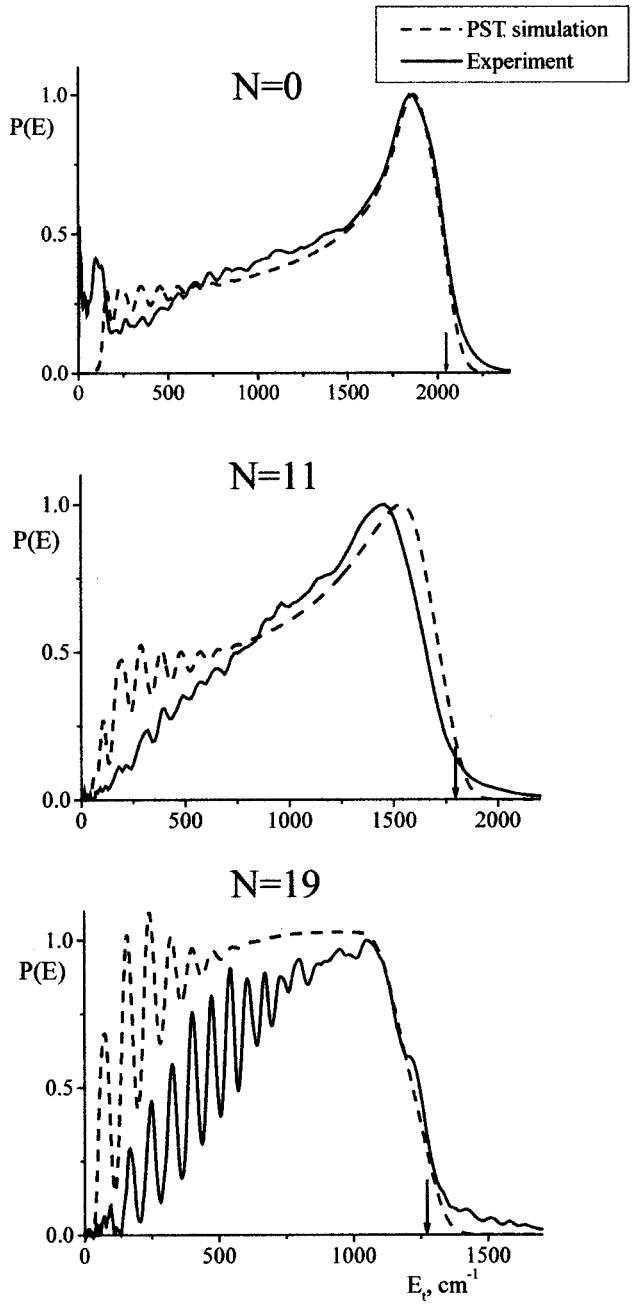

FIG. 3. Total c.m. translational energy E_t distributions of NO($A\,^2\Sigma^+, \nu=0, N=0,11,19$) obtained in photolysis of $(NO)_2$ at 213 nm (solid lines). The dashed lines show the corresponding PST simulations obtained with the impact parameter restricted to 2.6 Å. The arrows show the highest translational energies allowed for NO($A\,^2\Sigma^+, \nu=0, N=0,11,19$) which are 2038, 1774, and 1278 cm^{-1}, respectively.

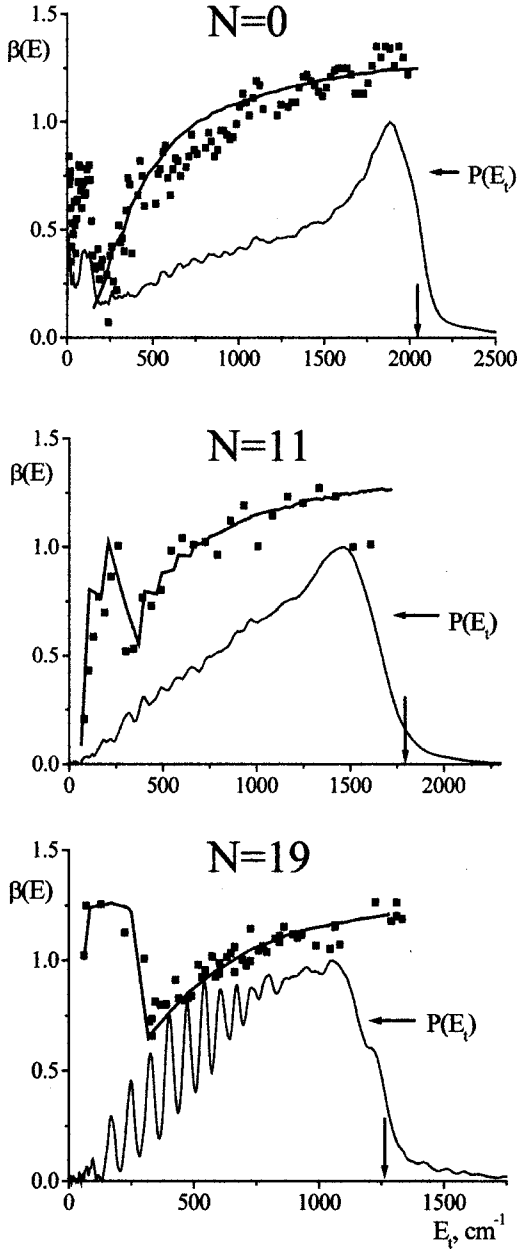

FIG. 4. Dependencies of the anisotropy parameter β_{eff} of NO($A\,^2\Sigma^+, \nu=0, N=0,11,19$) on the c.m. translational energy E_t (squares). The error in the measured values of the anisotropy parameter is typically ± 0.05. The solid lines through the data are the fits obtained by using the model described in the text. The corresponding energy distributions are also shown (solid lines). The arrows indicate the highest E_t allowed for NO($A\,^2\Sigma^+, \nu=0, N=0,11,19$).

and 19, except that the NO($X\,^2\Pi_{1/2,3/2}, \nu=1$) channel is energetically closed.

Figure 3 shows the $P(E_t)$ distributions for NO(A) in $N=0$, 11, and 19. The distinct peaks in the translational energy distributions correspond either to a specific NO(X) vibrational level, $\nu=0$ or 1 (in the $N=0$ image), or to high rotational levels of NO(X) $\nu=0$ (in the $N=11$ and 19 images).

In order to derive the dependence of β_{eff} on E_t, the angular distributions at each distance from the center (i.e., a particular speed) are fit to Eq. (3). The results are shown in Fig. 4. Note that each measured β_{eff} is a weighted average of the β parameters associated with the NO($X\,^2\Pi_{1/2,3/2}, \nu, J$) states whose E_{int} is complementary to E_t. In the case of NO($A, N=0$), β_{eff} depends on both the vibrational and rotational state of the NO($X, \nu=0,1, J$) cofragment. The dependence of β_{eff} on NO(X) rotational level is evident in the NO($A, N=11,19$) data where only NO($X, \nu=0$) is energetically allowed. The most remarkable feature in Fig. 4 is the similarity of the functional dependence of β on E_t for the three N values, despite the large differences in the energy available to the NO(X) products, and hence their corre-

sponding rovibrational distributions. In all three cases β_{eff} gradually decreases as E_t decreases, but then, at a specific low translational energy, it increases abruptly and later goes down again. The causes for the variation in β_{eff} are discussed in Sec. IV.

IV. CLASSICAL MODEL FOR NONAXIAL FRAGMENT RECOIL

A. Angular momentum conservation and transverse recoil

In a previous paper,[22] a model based on energy and angular momentum conservation was developed to explain the observed dependence of the recoil anisotropy parameter β_{eff} on the translational energy of recoiling fragments in the photodissociation of triatomic species whose transition dipole moment lies in the plane. According to this model, the rotation of the diatomic fragment during dissociation must be compensated by the orbital angular momentum of the departing fragments. Consequently, in the limit of small kinetic energy release and substantial rotational excitation of the diatomic fragment, the contributions from transverse recoil become large, and β deviates from its limiting values (2 and -1) even for infinitely fast dissociation. The model was applied successfully to the photoinitiated dissociation of a triatomic molecule (NO_2) and a van der Waals complex (ICl-Ne).[22]

We now extend this model to the more complicated case of a four-atomic species dissociating into two diatomic fragments. First, such dissociation is not necessarily planar, as out-of-plane motions are also possible. Second, unlike the case of jet-cooled triatomic dissociation for which the atomic fragment angular momentum is very small, here three angular momenta (i.e., those of the two diatomic fragments and the orbital angular momentum) can acquire any value provided that total angular momentum and energy are conserved. For NO dimer dissociation we obtain:

$$\mathbf{J}_{(\text{NO})_2}=\mathbf{J}_{\text{NO}(A)}+\mathbf{J}_{\text{NO}(X)}+\mathbf{L}, \tag{2}$$

$$E_{\text{avl}}=h\nu-D_0=E_{\text{int}}^{\text{NO}(A)}+E_{\text{int}}^{\text{NO}(X)}+E_t^{\text{NO}(A)}+E_t^{\text{NO}(X)}, \tag{3}$$

where D_0 is the dissociation threshold of channel I; $E_t^{\text{NO}(A,X)}$ are the c.m. recoil energies of the fragments; $E_{\text{int}}^{\text{NO}(A,X)}$ are the corresponding internal energies (i.e., vibrational, rotational, and spin–orbit energies); $\mathbf{J}_{(\text{NO})_2}$, $\mathbf{J}_{\text{NO}(A,X)}$ are the angular momenta of the parent $(\text{NO})_2$ molecule, and the NO(A,X) fragments; and $\mathbf{L}$ is the orbital angular momentum.

The orbital angular momentum $\mathbf{L}$ is due to the rotation of the c.m. of the recoiling fragments around the c.m. of the parent molecule and is predominantly directed perpendicular to the parent molecular plane. The latter means that only components of the fragments' angular momenta that are perpendicular to the parent molecular plane can be compensated by $\mathbf{L}$. For purely out-of-plane (helicopter-like) rotation $L \approx 0$, and $J_{\text{NO}(X)} \cong J_{\text{NO}(A)}$ must dominate in jet-cooled samples.

In our case, $J_{(\text{NO})_2}$ is determined by the rotational temperature of the parent, while $N_{\text{NO}(A)}=0,11,19$ are selected in the experiment. Since both $J_{(\text{NO})_2}$ and $J_{\text{NO}(A)}$ are known, $J_{\text{NO}(X)}$ must be related to L, as per Eq. (2). In the case of 3D dissociation (assuming $J_{(\text{NO})_2} \approx 0$) all values of L between $|J_{\text{NO}(A)}-J_{\text{NO}(X)}| \leqslant L \leqslant (J_{\text{NO}(A)}+J_{\text{NO}(X)})$ are possible, while in the case of purely planar dissociation $L=|J_{\text{NO}(A)} \pm J_{\text{NO}(X)}|$. The limiting values $|J_{\text{NO}(A)}-J_{\text{NO}(X)}|$ and $(J_{\text{NO}(A)}+J_{\text{NO}(X)})$ correspond, respectively, to fragments counterrotating and corotating in the parent molecular plane (see Fig. 5). Thus, for a fixed photolysis energy and $N_{\text{NO}(A)}$, high $J_{\text{NO}(X)}$ states must correlate with low c.m. recoil energies ($E_t=E_t^{\text{NO}(X)}+E_t^{\text{NO}(A)}$) and a high average L. For corotating fragments L may be very high.

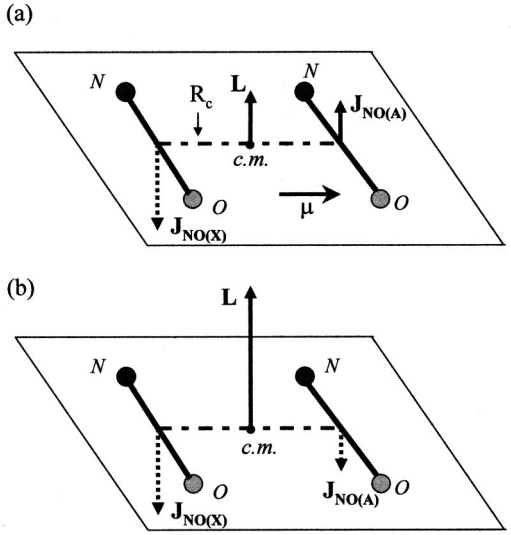

FIG. 5. The angular momentum vectors $\mathbf{J}_{\text{NO}(A)}$, $\mathbf{J}_{\text{NO}(X)}$, and $\mathbf{L}$ in planar dissociation of nonrotating NO dimer. In (a) the two fragments counterrotate in the plane, and their combined angular momentum can be compensated by a small value of $\mathbf{L}$. In (b), the corotating products result in $\mathbf{J}=|J_{\text{NO}(X)}+J_{\text{NO}(A)}|$, which must be compensated by a much larger $\mathbf{L}$. The critical distance Rc is the average distance between the c.m. of the fragments when dissociation occurs. The direction of the transition dipole moment μ is shown by an arrow.

There can be several reasons for the creation of highly rotating NO fragments in the dissociation. In direct dissociation, the anisotropy in the angular potential is usually the main source of torque, while in vibrational predissociation, the main source of diatom angular momentum is bending or torsional vibrations in the transition state. In the latter case, for example, the mapping of symmetric and antisymmetric bending levels can give rise to both corotating and counterrotating fragments, unless additional constraints are imposed (e.g., angular momentum constraint; see the following).

Irrespective of the source of angular momentum, the fundamental conservation laws must be obeyed, and they impose restrictions on product trajectories. In the c.m. coordinate system, the classical orbital angular momentum is given by

$$\mathbf{L}=m_{\text{NO}}\mathbf{r}_{\text{NO}(A)}\times\mathbf{V}_{\text{NO}(A)}+m_{\text{NO}}\mathbf{r}_{\text{NO}(X)}\times\mathbf{V}_{\text{NO}(X)}, \tag{4}$$

where $\mathbf{r}_{\text{NO}(X,A)}$ is a vector directed from the c.m. of $(\text{NO})_2$ to the c.m. of the NO(X,A) fragments, and $\mathbf{V}_{\text{NO}(X,A)}$ is the c.m. velocity of NO(X,A). Angular momentum conservation dictates that

$$|\mathbf{L}|=|m_{\text{NO}}\mathbf{R}\times\mathbf{V}_{\text{NO}}|=m_{\mathbf{NO}}\cdot R\cdot V_{\text{NO}}\cdot \sin\varphi, \tag{5}$$

where R is the distance between the center-of-masses of the departing NO(A) and NO(X) fragments ($\mathbf{R}=\mathbf{r}_{NO(X)}-\mathbf{r}_{NO(A)}$), and φ is the angle between $\mathbf{R}$ and $\mathbf{V}_{NO}$. If we define axial recoil as the direction of recoil of the diatomic fragments with no rotational angular momentum, then this direction must coincide with $\mathbf{R}$.[22] Using, $|\mathbf{L}|=\hbar\cdot\sqrt{L\cdot(L+1)}$, and $E_t=E_{avl}-E_{int}^{NO(A)}-E_{int}^{NO(X)}$, the relation between the recoil angle φ and the translational energy of diatomic fragments can be expressed as

$$\sin^2\varphi=\frac{\hbar^2 L\cdot(L+1)}{R_C^2\cdot m_{NO}\cdot(E_{avl}-E_{int}^{NO(A)}-E_{int}^{NO(X)})}. \tag{6}$$

Here R_C is a critical interfragment distance where the rotational and orbital angular momenta become established. Its value can be loosely related to the value of R at the transition state; i.e., $R_C \geqslant R_{TS}$. Note that we treat R_C as the distance between the center-of-masses of the two NO fragments, rather than as the N–N bond length, since at this distance we assume that the N–N bond is already broken.

The angle φ is related to the recoil anisotropy parameter β by

$$\beta=2\cdot P_2(\cos\varphi). \tag{7}$$

From Eq. (6) it is evident that at each E_{avl}, a specific combination of fragments' quantum states ($\mathbf{J}_{NO(A)},\mathbf{J}_{NO(X)}$) and orbital momentum $\mathbf{L}$ will be associated with a distinct transverse recoil angle φ, and the deviations from axial recoil will increase with increasing E_{rot} of NO(X). For each ($\mathbf{J}_{NO(A)},\mathbf{J}_{NO(X)}$) pair, however, several L values are possible, e.g., $|J_{NO(A)}-J_{NO(X)}|\leqslant L\leqslant(J_{NO(A)}+J_{NO(X)})$ for 3D dissociation, and $L=|J_{NO(A)}\pm J_{NO(X)}|$ for planar dissociation. We note that (i) although the measured anisotropy parameter is an average over all possible $\beta(J_{NO(A)},J_{NO(X)},L)$, for $J_{NO(X)}\gg J_{NO(A)}$ the allowed L values cluster around the value of $J_{NO(X)}$, and therefore large deviations from axial recoil are expected for high E_{rot} of NO(X); (ii) the variation of β with E_t depends on the particular dissociation geometry, i.e., whether or not it is confined to a plane (see the following); and (iii) in accordance with angular momentum conservation, for a given E_{avl}, $J_{NO(A)}$, and R_C, the condition

$$E_t\geqslant\frac{\hbar^2\cdot L\cdot(L+1)}{2\cdot m_{NO}\cdot R_C^2} \tag{8}$$

must be satisfied, which constrains the maximum allowed value of L for a particular pair ($J_{NO(X)},J_{NO(A)}$).

B. Application of the model

The above-described model is general, but its implementation is not always straightforward, because the geometrical configuration at which it is applied is ill defined. In particular, the use of R_C is approximate and its value is unknown, and must be either inferred from fits to the data or obtained from calculations. Also, we do not know *a priori* whether or not the dissociation is confined to the plane.

Simulations of the variation of $\beta_{eff}(E_t)$ obtained from the NO(A,N) images were performed as follows. From the E_t distribution for each image, $E_{rot}^{NO(X)}$ was generated by energy conservation. The NO(X) rotational state distributions that best fit $E_{rot}^{NO(X)}$ (after convolution with the instrument resolution function) were derived next (see Sec. V), and the β_{eff} values were finally calculated as the weighted averages of the individual β values of those NO J states, whose energies correspond to E_t values that fall within a small range ΔE_t.[33] The L values allowed by Eqs. (2), (3), and (8) were determined for planar dissociation by using R_C as a fit parameter. Since the maximum measured recoil anisotropy ($\beta_{eff}=1.36\pm0.05$) was less than the limiting value ($\beta=2$), the final anisotropy was scaled to provide a best fit to the experimental data. Possible causes for the reduction in the maximum anisotropy value are discussed in Sec. V. The best fits of the anisotropy dependencies were achieved by assuming planar dissociation and $R_C=2.6\pm0.4$ Å, and are shown in Fig. 4.

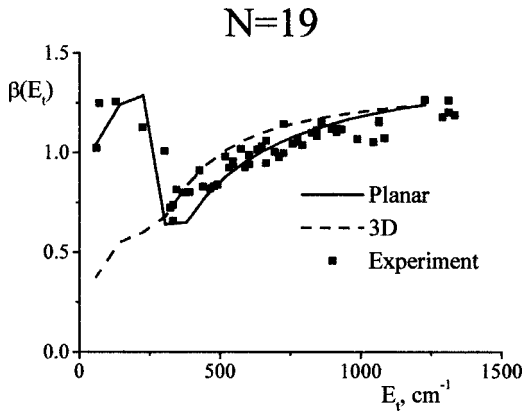

FIG. 6. Comparison of simulations of the change in the anisotropy parameter β_{eff} with translational energy (E_t) for the case of 3D (dashed line) and planar (solid line) dissociation. The corresponding experimental dependence $\beta_{eff}(E_t)$ for $N=19$ is depicted with squares. The abrupt increase in β_{eff} observed at low E_t is reproduced only by assuming planar dissociation. See the text for details.

The increase in β_{eff} near the threshold for the opening of $\nu=1$ observed in the NO($A,N=0$) image illustrates that for the same $E_{int}^{NO(X)}$, fragments generated in $\nu=1$ have much less rotational excitation than those in $\nu=0$, and therefore give rise to higher values of β. Such behavior has been observed before in the photodissociation of NO_2.[22]

The abrupt increase of β at small translational energies observed in the $N=11$, 19 images has a different origin. It is caused by the fact that at low fragments' translational energies, the high L values that correspond to *corotating* fragments become energetically forbidden [cf. Eq. (8)]. In planar dissociation, only two values, $L_-=|J_{NO(A)}-J_{NO(X)}|$ and $L_+=|J_{NO(A)}+J_{NO(X)}|$, are possible for each ($J_{NO(A)},J_{NO(X)}$) pair (assuming parent $J\cong0$), and the corresponding anisotropy parameter β_{eff} is an average of the values corresponding to L_- and L_+, with the higher L resulting in a smaller value of β_{eff}. Evidently, the exclusion of fragments with the smaller β values results in a substantial increase in the observed value of β_{eff}. In contrast, when all values of L between L_+ and L_- are allowed (i.e., when the dissociation is not confined to a plane), this becomes only a minor effect, as shown in Fig. 6. We conclude that the increase of β_{eff} at very low E_t is merely a manifestation of angular momentum constraints in planar dissociation that allows the formation of only counterrotating products.

V. DISCUSSION

A. Angular distributions of NO fragments: Variation of β_{eff}

Unlike the well-characterized ground state of $(NO)_2$, very little is known about its electronically excited states. Nevertheless, according to molecular orbital analysis and *ab initio* calculations the transition dipole moment of the $^1B_2 \leftarrow {}^1A_1$ UV system lies in the molecular plane, parallel to the N–N bond.[15–17] This geometry corresponds to a limiting value of $\beta=2$, whereas the maximum value of the anisotropy parameter, $\beta_{\max}=1.36\pm0.05$, measured at high E_t for nonrotating products is much smaller.

Several factors can lead to a reduction in the limiting value of β,[34] among them: (i) simultaneous excitation of parallel and perpendicular transitions; (ii) parent rotation during dissociation (lifetime effect); (iii) out-of-plane motions of the dissociating molecule; (iv) deviations from axial recoil due to in-plane motions; and (v) contributions from background signals with low β values.

If an out-of-plane perpendicular transition is also excited, it is expected to add a constant negative contribution to β, which is independent of E_t, and will therefore reduce β_{eff} equally for all fragment speeds. However, neither experiment nor theory support the existence of a perpendicular transition correlated with NO(A). Moreover, the contribution of such transition is expected to change as the excitation wavelength is varied, but measurements of β in the range 193–220 nm do not reveal a large variation.[17,35] An in-plane perpendicular transition would not result in the observed dependence of β_{eff} on E_t, as it would contribute values of β_{eff} ranging from -1 at large E_t to positive ones at small E_t.[22,36]

Parent rotation during dissociation is known to cause a reduction in β. When the dissociation is not infinitely fast on the time scale of parent rotation, the parent may rotate through an angle $\psi=\omega\langle\tau\rangle$ prior to dissociation, where ω is the angular velocity of rotation of the parent molecule and $\langle\tau\rangle$ is its average lifetime. In the case of a dissociating diatomic this leads to the well-known expression,[37]

$$\beta(E_t)=\frac{1+(\omega\langle\tau\rangle)^2}{1+4\cdot(\omega\langle\tau\rangle)^2}. \tag{9}$$

Taking into consideration the rotational temperature of the parent (3–5 K), this formula gives $\langle\tau\rangle=1.8-2.0$ ps for $\beta=1.33-1.41$. The measured buildup time of NO(A) at 210 nm is $\tau\approx1$ ps,[18] which corresponds to $\beta\approx1.70$, clearly higher than the measured value. Using the classical method of Yang and Bersohn gives similar results.[38] Since the product buildup time has been measured at 210 nm, we have checked to see whether the maximum value of β depends on excitation energy. At 216 and 220 nm, the measured values are 1.30 ± 0.05 and 1.16 ± 0.05, respectively, which would correspond at most to a modest increase in lifetime. We conclude that lifetime reduction contributes to the reduction in β, but it is not the only factor.

The above-mentioned treatment uses a classical (or semiclassical) approach to parent rotation, which has its limitations, especially for the case of small parent rotational quantum numbers.[39] However, considering that the measured decay time of the excited electronic state of the $(NO)_2$ electronic transition under study is $\tau\sim0.3$ ps,[19] the rotational structure in the upper state is unresolved, and a wave packet of rotational states is excited. The evolution of this wave packet in time is the origin of the effect of parent rotation on the anisotropy, as described by Eq. (9).

The effect of out-of-plane motion in the dissociation on β is harder to evaluate. Such motions may be a result of a symmetry requirement for surface crossing, Franck–Condon overlap, or vibrational energy flow during dissociation. They may contribute here as well.

The value of β can also be reduced if rotation of the recoil axis takes place during the dissociation due to the evolution of the molecular geometry. This may happen, for example, if the geometry of the electronically excited state differs substantially from that of the ground state, as happens in the case NO_2 photodissociation.[22] Recall that $\beta=2.0$ can be obtained for nonrotating fragments only when both the transition dipole moment μ_ϵ and R lie parallel to the a axis of a prolate top. When R deviates from the a axis, $\beta<2.0$ will be obtained even for fast dissociation generating nonrotating fragments.[22]

Additionally, we cannot exclude the possibility that a small background signal whose β is small leads to some reduction in β_{eff}. As discussed previously, background subtraction is essential to the data processing, and although done carefully, a small reduction in β due to this factor cannot be totally excluded.

In conclusion, it is clear that some of the reduction in the maximum value of β for nonrotating products is due to the finite dissociation lifetime. Out-of-plane motions and rotation of the recoil axis due to the evolution of the molecular geometry during the dissociation are likely causes of further reduction. Contamination from signals with lower β values cannot be definitively excluded, but is expected to make only a minor contribution. In contrast, for highly rotating fragments, the large reduction in β is caused by the transverse recoil component in planar dissociation, as described in Sec. IV.

When comparing the simulated and measured distributions of β_{eff} as a function of E_t, it must be borne in mind that for low NO(X) rotational levels (high E_t), no change in β is expected. It is only by examining the region of high NO(X) rotational states (low E_t) that the mechanistic origin of the β variation can be inferred. Our study shows that the high J states of NO(X) must be produced via planar dissociation. For low NO(X) rotational states, our work cannot distinguish between planar and nonplanar dissociation events, or between corotating and counterrotating fragments.

The β_{eff} distributions obtained from images of low and high N states of NO(A) can all be fit by using $R_C=2.6$ Å ±0.4, which places the transition state (TS) at an internuclear distance close to the equilibrium N–N distance in the ground state (2.26 Å). Therefore, the TS can be considered ''tight,'' i.e., it has a vibrational structure. In such a case, the projection (mapping) of symmetric and antisymmetric in-plane bending wave functions into NO angular momentum states will give rise to both corotating and counterrotating fragments. Only for very highly rotating NO fragments,

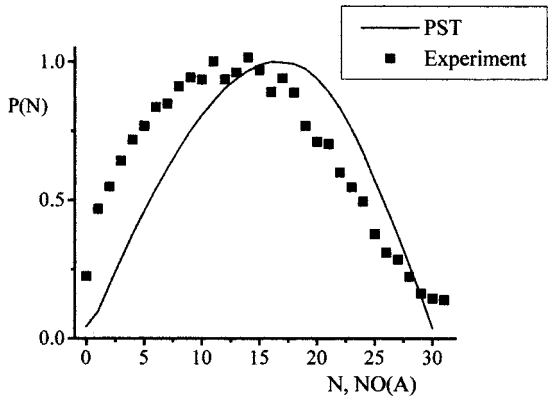

FIG. 7. Rotational energy distribution of NO($A,\nu=0$) fragments after 213 nm photolysis ($E_{avl}=2038\ cm^{-1}$).

would the production of corotating products become forbidden by angular momentum constraints [Eq. (8)]. On the other hand, the repulsive forces between the fragments already start to act near the Franck–Condon region. In such a situation, the angular anisotropy of the potential energy surface, and in particular the coupling between the angular and the dissociative N–N coordinates, are expected to influence the final state distributions as well, causing deviations from statistical behavior (see the following).

It is also worth noting that the model presented here is in agreement with the results of Naitoh *et al.* obtained with 193 nm photolysis.[17] These authors inferred the value of β_{eff} from Doppler profiles of selected N states of NO(A) in the range $N=7-23$, and found that the *average* β_{eff} value *increased* for higher N states. Recall that with jet-cooled samples, $\mathbf{L}\cong\mathbf{J}_{NO(A)}+\mathbf{J}_{NO(X)}$, and the fragments have a broad rotational state distribution extending to the energetic limit ($J_{NO(X)}\leqslant 60$).[17] The peak in the Doppler profile corresponds to low fragment velocities [i.e., to high J states of NO(X)], resulting in, on average, a large deviation from axial recoil, and a small average β_{eff}. As the N level of the monitored NO(A) state increases (but is still not too high), the maximum allowed NO(X,J) level decreases, and therefore the average β_{eff} should increase, as indeed observed.[17]

B. Correlated energy distributions

This paper is concerned with the stereodynamical aspects of $(NO)_2$ photodissociation, while the corresponding scalar properties (correlated energy distributions) will be the subject of a separate report. Here we comment only on those dynamical aspects that follow from the anisotropy measurements.

The global rotational state distributions of the NO(A,ν) fragments measured before at 193 nm were fit by a constrained version of PST, in which restrictions due to preferred in-plane dissociation for higher N's were included.[18] The relative contribution of in- and out-of-plane motions was adjusted for each NO(A) rotational state until a fit to the data was obtained. Such a fit was carried out for vibrational levels $v=0-2$. The unconstrained PST distributions underestimated the contributions of low NO(A) rotational states, relative to the higher ones. The global NO(A) rotational state distribution measured by us at 213 nm and shown in Fig. 7 is also colder than predicted by PST.

The picture that emerges from the NO(A) images recorded at 213 nm is that the NO(X) rotational distributions correlated with specific NO(A) N states also deviate from statistical (PST) predictions. Most noticeably, the population of high NO(X) rotational levels is always overestimated by PST compared to the experiment. Since unconstrained PST did not give a good fit, we used an impact parameter constraint in which the maximum impact parameter was 2.6 Å, the interfragment separation that best fits the anisotropy data. This somewhat reduced the population of high J states, but the fit still was not satisfactory (Fig. 3).

Assuming that the dissociation is constrained entirely to the molecular plane for all rotational states makes the agreement poorer. The failure of PST to describe the rotational distribution is not surprising, since the dissociation involves a rather tight TS, a situation for which PST does not apply.

In order to obtain the correlated NO(X) rotational distributions, the speed distributions were fit by a set of Gaussian functions, each centered at the position of a NO($X\,^2\Pi_{1/2,3/2},J$) state. The widths of the Gaussian functions were optimized to give the best fit for each speed distribution. The relative populations of the J states were then determined by a least-squares fit, using Tikhonov regularization to stabilize the coefficients in the overlapped region of low J states. This procedure, which was found to be stable and superior to iterative methods, is similar to the one used in the image reconstruction.[31] Because of the small separation between low J states ($J\leqslant 5$) in the energy distribution, the accuracy of extraction of their populations is rather low ($\pm 20\%$), while for higher J's it is about $\pm 5\%$. The extracted rotational distributions show that the two spin–orbit states of NO(X) are approximately equally populated in all the correlated distributions. Therefore, in the rotational state distributions shown in Fig. 8, which are compared to PST predictions, the spin–orbit levels were suppressed for clarity of presentation.

Inspection of Fig. 8 reveals that the rotational state distributions are not described well by PST, and appear to exhibit signatures of exit channel dynamics. The distributions are likely to include contributions from one or more of the following sources: (i) mapping of TS wave functions (bending and torsional) into fragment rotations; (ii) exit-channel repulsion and the angular anisotropy in the potential energy surface; and (iii) rotational energy flow beyond the TS.[40] The nature of the dynamical forces can be clarified by extending the measurements to photolysis wavelengths closer to the threshold of reaction I, and such measurements are currently in progress.

VI. SUMMARY

(1) A classical model that describes quantitatively the deviations from axial recoil in photodissociation of triatomic species is applied to the dissociation of the tetra-atomic, weakly bound molecule $(NO)_2$. It is shown that the deviations are governed by the conservation of angular momentum.

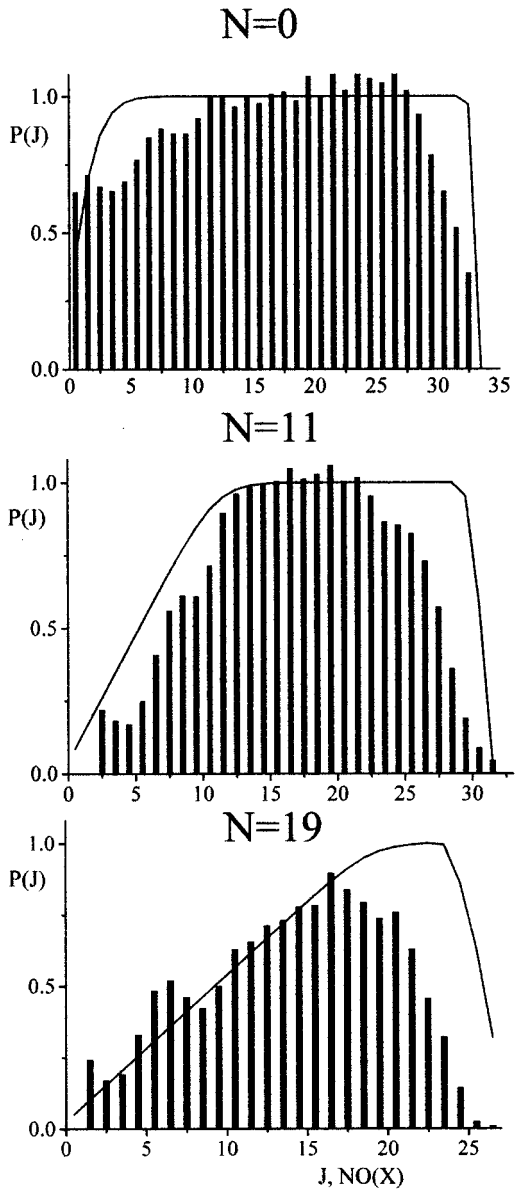

FIG. 8. Correlated distributions P(J) of NO(X,J) states extracted from the observed energy distributions P(E_t) (see Fig. 3) for NO($A,N=0,11,19$) are given as a bar graph. The corresponding PST distributions are shown for comparison (solid line).

(2) The application of the model to the 213 nm photodissociation of $(NO)_2$ describes well the dependence of β_{eff} on NO(X,J) for the monitored NO($A,\nu=0,N$) levels. The best fit in all cases is obtained at an interfragment separation of $R_C=2.6\pm0.4$ Å, close to the N–N distance in the ground state (2.26 Å). For high rotational levels of NO(X), the dissociation must take place in the plane, and it produces both corotating and counterrotating NO fragments, possibly as a result of mapping of symmetric and antisymmetric transition state wave functions into product rotational states. For the highest allowed J states, due to angular momentum constraints, only counterrotating products are allowed.

(3) The correlated NO(X) distributions and the global NO(A) distribution cannot be fit by constrained PST. The dissociation takes place via a tight TS, and exit-channel effects likely influence the final rotational state distributions.

ACKNOWLEDGMENTS

Support by the National Science Foundation and the Donors of the Petroleum Research Fund, administered by the American Chemical Society is gratefully acknowledged. The authors benefited greatly from discussions with Albert Stolow, Carl Hayden, and David W. Chandler.

[1] R. J. Bernish, M. Wu, and R. E. Miller, Faraday Discuss. **97**, 57 (1994); L. Oudejans, R. E. Miller, and W. L. Hase, *ibid.* **102**, 323 (1995), and references therein.
[2] Y. Rudich and R. Naaman, J. Chem. Phys. **96**, 8618 (1992).
[3] A. L. L. East, J. Chem. Phys. **109**, 2185 (1998); A. L. L. East and J. K. G. Watson, *ibid.* **110**, 6099 (1999).
[4] C. M. Western, P. R. R. Langridge-Smith, B. J. Howard, and S. E. Novick, Mol. Phys. **44**, 145 (1981).
[5] S. G. Kukolich, J. Mol. Spectrosc. **98**, 80 (1983).
[6] M. P. Casassa, J. C. Stephenson, and D. S. King, J. Chem. Phys. **89**, 1966 (1988).
[7] J. R. Hetzler, M. P. Casassa, and D. S. King, J. Phys. Chem. **95**, 8086 (1991); E. A. Wade, J. I. Cline, K. T. Lorenz, C. Hayden, and D. W. Chandler, J. Chem. Phys. **116**, 4755 (2002).
[8] Y. Matsumoto, Y. Oshima, and T. Michio, J. Chem. Phys. **92**, 937 (1990).
[9] Ph. Brechignac, S. De Benedictis, N. Halberstadt, B. J. Whitaker, and S. Avrillier, J. Chem. Phys. **83**, 2064 (1985).
[10] M. P. Casassa, J. C. Stephenson, and D. S. King, J. Chem. Phys. **85**, 2333 (1986).
[11] H. J. Bernstein and G. Herzberg, J. Chem. Phys. **15**, 77 (1947).
[12] J. Billingsley and A. B. Callear, Trans. Faraday Soc. **67**, 589 (1971).
[13] E. Forte and H. Van Den Berg, Chem. Phys. **30**, 325 (1978).
[14] O. Kajimoto, K. Honma, and T. Kobayashi, J. Phys. Chem. **89**, 2725 (1985).
[15] Y. Naitoh, Y. Fujimura, and O. Kajimoto, Chem. Phys. Lett. **190**, 135 (1992).
[16] Y. Naitoh, Y. Fujimura, K. Honma, and O. Kajimoto, Chem. Phys. Lett. **205**, 423 (1993).
[17] Y. Naitoh, Y. Fujimura, K. Honma, and O. Kajimoto, J. Phys. Chem. **99**, 13652 (1995).
[18] O. Kajimoto, Progr. Theor. Phys. Suppl. **116**, 167 (1994).
[19] V. Blanchet and A. Stolow, J. Chem. Phys. **108**, 4371 (1998).
[20] C. C. Hayden and A. Stolow (private communication).
[21] R. N. Zare and D. R. Herschbach, Proc. IEEE **51**, 173 (1963).
[22] A. V. Demyanenko, V. Dribinski, H. Reisler, H. Meyer, and C. X. W. Qian, J. Chem. Phys. **111**, 7383 (1999).
[23] A. Sanov, Th. Droz-Georget, M. Zyrianov, and H. Reisler, J. Chem. Phys. **106**, 7013 (1997).
[24] D. H. Parker and A. Eppink, J. Chem. Phys. **107**, 2357 (1997); Rev. Sci. Instrum. **68**, 3477 (1997).
[25] K. P. Huber and G. Herzberg, *Molecular Spectra and Molecular Structure*, Constants of Diatomic Molecules, Vol. VI (Van Nostrand Reinhold, New York, 1979).
[26] M. W. Feast, Can. J. Res., Sect. A **28**, 488 (1950); G. Meijer, M. Ebben, and J. J. ter Meulen, Chem. Phys. **127**, 173 (1988); A. Timmermann and R. Wallenstein, Opt. Commun. **39**, 239 (1981).
[27] J. C. Miller and R. N. Compton, J. Chem. Phys. **84**, 675 (1986).
[28] M. N. R. Ashfold, R. N. Dixon, J. D. Prince, B. Tutcher, and C. M. Western, J. Chem. Soc., Faraday Trans. 2 **82**, 1257 (1986).
[29] I. Fischer, A. Strobel, J. Staecker, G. Niedner-Schatteburg, K. Müller-Dethlefs, and V. Bondybey, J. Chem. Phys. **96**, 7171 (1992).
[30] Probed $A\ ^2\Sigma^+$ (as well as the intermediate $E\ ^2\Sigma^+$) state belongs to Hund's case b, i.e., the rotational and spin–orbit motions are uncoupled. The rotational energy is best described by the ''good'' quantum number N, $E_{\text{rot}}=B\cdot N\cdot(N+1)$ (ignoring the spin–rotational splitting). As a consequence, in the $E\ ^2\Sigma^+\leftarrow A\ ^2\Sigma^+$ transition, an $A\ ^2\Sigma^+$ state with a specific N (and two different $J=N\pm1/2$) is probed.
[31] V. Dribinski, A. Ossadtchi, V. Mandelshtam, and H. Reisler, Rev. Sci. Instrum. (in press).
[32] B. J. Whitaker, in *Imaging in Chemical Dynamics*, edited by A. G. Suits and R. E. Continetti [ACS Symp. Ser. **770**, 68 (2001)].
[33] The spin–orbit states of NO were suppressed in the simulations of β_{eff}.
[34] G. E. Busch and K. R. Wilson, J. Chem. Phys. **56**, 3638 (1972).
[35] A. V. Demyanenko, V. Dribinski, A. B. Potter, and H. Reisler (unpublished).

[36] D. H. Mordaunt, M. N. R. Ashfold, and R. N. Dixon, J. Chem. Phys. **104**, 6460 (1996).
[37] C. Jonah, J. Chem. Phys. **55**, 1915 (1971).
[38] S. Yang and R. Bersohn, J. Chem. Phys. **61**, 4400 (1974).
[39] T. J. Butenhoff, K. L. Careton, R. D. van Zee, and C. B. Moore, J. Chem. Phys. **94**, 1947 (1991).
[40] R. Schinke, *Photodissociation Dynamics*, (Cambridge University Press, Cambridge, 1993).